Available online at www.sciencedirect.com

ScienceDirect

www.elsevier.com/locate/jes

JES JOURNAL OF ENVIRONMENTAL SCIENCES

www.jesc.ac.cn

Research Article

Development of MoS_2-stainless steel catalyst by 3D printing for efficient destruction of organics via peroxymonosulfate activation

Yufeng Liu[1], *Jianhui Xu*[1,*], *Xin Fu*[1], *Pengxu Wang*[1], *Dan Li*[1,*], *Yunfei Zhang*[1], *Shenggui Chen*[2,3,4], *Chunhui Zhang*[1], *Peng Liu*[1]

[1] *School of Environment and Civil Engineering, Dongguan University of Technology, Dongguan 523808, China*
[2] *School of Art and Design, Guangzhou Panyu Polytechnic, Guangzhou 511483, China*
[3] *Dongguan Institute of Science and Technology Innovation, Dongguan University of Technology, Dongguan 523808, China*
[4] *School of Mechanical Engineering, Dongguan University of Technology, Dongguan 523808, China*

ARTICLE INFO

Article history:
Received 5 December 2022
Revised 14 January 2023
Accepted 17 January 2023
Available online 25 January 2023

Keywords:
3D printing
Stainless steel
MoS_2
Peroxymonosulfate activation
Degradation mechanism

ABSTRACT

Herein, a novel MoS_2-stainless steel composite material was first synthetized via a 3D printing method (3DP MoS_2-SS) for peroxymonosulfate (PMS) activation and organics degradation. Compared with MoS_2-SS powder/PMS system (0.37 g/(m^2/min)), 4.3-fold higher k_{FLO}/S_{BET} value was obtained in 3DP MoS_2-SS/PMS system (1.60 g/(m^2/min), resulting from the superior utilization of active sites. We observed that 3DP MoS_2-SS significantly outperformed the 3DP SS due to the enhanced electron transfer rate and increased active sites. Moreover, Mo^{4+} facilitated the Fe^{2+}/Fe^{3+} cycle, resulting in the rapid degradation of florfenicol (FLO). Quenching experiments and electron paramagnetic resonance spectra indicated that •OH, SO_4•$^-$, O_2•$^-$ and $^1O_2$ were involved in the degradation of FLO. The effect of influencing factors on the degradation of FLO were evaluated, and the optimized degradation efficiency of 98.69% was achieved at 1 mM PMS and pH of 3.0. Six degradation products were detected by UPLC/MS analyses and several possible degradation pathways were proposed to be the cleavage of C-N bonds, dechlorination, hydrolysis, defluorination and hydroxylation. In addition, 3DP MoS_2-SS/PMS system also demonstrated superior degradation performance for 2-chlorophenol, acetaminophen, ibuprofen and carbamazepine. This study provided deep insights into the MoS_2-SS catalyst prepared by 3DP technology for PMS activation and FLO-polluted water treatment.

Introduction

Recently, advanced oxidation processes (AOPs) based on peroxymonosulfate (PMS) activation attracted considerable eyesight for the green remediation of organic contaminants in

* Corresponding authors.
E-mails: 2017052@dgut.edu.cn (J. Xu), lid@dgut.edu.cn (D. Li).

https://doi.org/10.1016/j.jes.2023.01.016
1001-0742/

wastewater (Chu et al., 2021; Ding et al., 2020). The activation of PMS could be achieved by alkaline, heat, ultraviolet, ultrasonic and electrochemical method (Gao et al., 2022; Son et al., 2021). However, these methods were restricted for practical application by high energy consumption and low activated efficiency. Compared with other methods, Fe-based transition metals materials were supposed to be the excellent approach for PMS activation due to its high efficiency, low cost and environmental friendliness (Huang et al., 2019; Zhou et al., 2018). For example, Cao et al. (2019) indicated that zero-valent iron (ZVI) activated PMS for efficient degradation of tetracycline with a high degradation efficiency of 88.5% in 5 min. Nevertheless, the formation of iron oxide and hydroxide on the surface resulting from the corrosion of iron would extremely decrease its feasibility and applicability (Pang et al., 2019). Although a number of strategies such as pretreatment methods, physical and chemical technology were applied to enhance the reactivity of Fe-based catalyst, the complex preparation procedure, expensive price and specific application environment significantly limited for further application (Huo et al., 2020; Zhang et al., 2022b). Therefore, to develop an efficient, stable and cheap Fe-based catalyst was of great urgency.

Stainless steel (SS) was widely applied for scaled-up applications in various fields due to its superior corrosion resistance, abrasion resistance and mechanical stability (Bahmani-Oskooee et al., 2017; Zhang et al., 2019a). More importantly, it was composed of abundant metal elements, especially Fe, Cr, Mn and etc. Previous studies indicated that multimetallic catalysts would accelerate PMS activation and organics degradation due to the enhanced adsorption performance and electron-transfer capability (Fu et al., 2015; Wang et al., 2022a; Zhou et al., 2016). Thus, SS shows great potential to be an excellent catalyst owing to the above advantages. However, SS exhibits relatively insufficient active sites for catalytic reaction (Yao et al., 2020). The strategy to regulate electronic structure and increase the active sites of SS were desirable. As a transitions-mental dichalcogenides, MoS_2 was extensively used in photocatalytic and electrocatalytic fields owing to the abundant active sites, large specific surface area and fast electron transfer (Chen et al., 2022; Liang et al., 2021; Shi et al., 2017; Yang et al., 2021a). Zhang et al. (2019b) demonstrated that the loading of MoS_2 on SS exhibited superior HER activity and stability relative to commercial carbon cloth. Besides that, the exposed Mo sites on the catalyst surface were reported to significantly facilitate the cycle of Fe^{3+}/Fe^{2+} electron pair (Yi et al., 2019). Thus, the introduction of MoS_2 might be an effective strategy to increase the active sites and improve the catalytic performance of SS for PMS activation toward organics degradation.

Most of the powder catalysts for PMS activation suffered from the shortcomings of difficult recovery and secondary pollution (Zhang et al., 2022a). In addition, Nano and micron-scale powder catalysts would immediately agglomerate once it was placed in the reaction solution, which prevented the contact between powder catalyst and organics and resulted in the low degradation efficiency of organics (Wang et al., 2022a). Therefore, it was desirable to develop a catalyst with high efficiency, low cost and easy recovery. 3D printing (3DP) method was an emerging approach to fabricate the catalyst, which could minimize the consumption of raw materials and reduce the preparation steps (Lee et al., 2017; Sullivan et al., 2021; Yang et al., 2023). Compared with conventional fabrication procedure, catalysts manufactured by 3DP method demonstrated excellent reusability and easy recovery (Yang et al., 2021b). Our previous study also indicated that 3DP MoS_2/Ni cathode possessed excellent dechlorination of florfenicol and long-term stability compared with that prepared by the hydrothermal method (Xu et al., 2022b). Most especially, 3DP also could regulate the shape, size through a simple computer model. Li et al. reported a highly ordered Ti-based boron-doped diamond (BDD) electrode synthesized by 3D printing method could provide more reaction active sites and achieve superior degradation of organics relative to 2D BDD electrode (Li et al., 2021b). Therefore, it is a promising strategy to manufacture catalyst by 3DP technology. To the best of our knowledge, the MoS_2-SS composite catalyst manufactured via 3D printing method have not reported and the efficiency by MoS_2-SS catalyst for PMS activation and organics degradation remain unclear. Furthermore, a detailed understanding on the comparison between powder catalyst and massive catalyst synthesized by 3DP method for PMS activation and organics degradation are insufficient. The research on the aspects was needed and clarifying the involved mechanisms would broaden the practical application prospects of 3D printing technology for the catalyst fabrication and wastewater treatment.

Herein, we rationally designed a novel MoS_2-stainless steel composite material via a 3D printing method (3DP MoS_2-SS), and employed for PMS activation and organics degradation. The microstructure and electron transfer capability of 3DP MoS_2-SS were characterized systematically. Florfenicol was selected as the target organics, which was deemed as one of the most widely used veterinary antibiotics in China (Ma et al., 2021). We compared the degradation efficiency of FLO in 3DP MoS_2-SS/PMS and MoS_2-SS powder/PMS systems. Quenching experiments, electron paramagnetic resonance (EPR) measurement and amperometric current-time curve were conducted to explore the mechanism of PMS activation by 3DP MoS_2-SS. The influencing factors (the doping content of MoS_2, PMS dosage and initial pH) for the FLO degradation were evaluated, and the possible degradation pathways were proposed based on the identification of degradation products by ultraperformance liquid chromatography/mass spectrometry (UPLC/MS) analysis. The variation of total organic carbon (TOC), aqueous inorganic anion (Cl^-, F^-) during the degradation of FLO were investigated. In addition, we also evaluated the recycle experiments for the degradation of FLO by 3DP MoS_2-SS. This study could provide novel insights into the rational design of MoS_2-SS catalyst through 3D printing technology for PMS activation toward organics degradation.

1. Materials

1.1. Chemical

Pristine SS powder (30-50 μm, 99%,) that customized for 3D printing technology were purchased from Avimetal Powder Metallurgy Technology Co., Ltd. (Beijing, China). MoS_2 powder (99.5%, < 2 μm), florfenicol (FLO, 98%), peroxymonosulfate (PMS, $2KHSO_5 \bullet KHSO_4 \bullet K_2SO_4$), acetaminophen (ACT, > 98%),

tert-butyl alcohol (TBA, 99.5%), methanol (MeOH, > 99.9%), L-histidine (99%) and 4-hydroxy-2,2,6,6-tetramethylpiperidine (TEMP, > 97%) were purchased from Aladdin Chemical Reagent Co., Ltd. (Shanghai, China). Ibuprofen (IBP, > 98%), 2-chlorophenol (2-CP, 99%), 1,4-benzoquinone (BQ, 99%), 5,5-dimethyl-1-pyrroline-noxide (DMPO, > 99%), carbamazepine (CBZ, 99%) were purchased from Macklin Chemical Reagent Co., Ltd. (Shanghai, China).

1.2. *Fabrication of 3DP SS and 3DP MoS_2-SS*

The overall fabrication processes of the 3DP SS and 3DP MoS_2-SS by 3D printing technology were based on our previous work (Xu et al., 2022b) and the detailed schematic illustration was presented in **Appendix A Fig. S1**. Briefly, the mixed MoS_2-SS powders with different mass ratios (0%, 3%, 5%, 8%, 10%) were mechanically synthesized by a planetary ball milling (QM-3SPOP4, NanDa Instrument Plant, China). The milling time and rotation speed were set as 3 hr and 400 r/min, respectively. The mixed powders after ball milling would be filtered through 200 mesh screen. Subsequently, 3DP SS and 3DP MoS_2-SS catalysts could be obtained after the 3D printing process.

1.3. *Experimental procedure*

The degradation experiments of FLO were conducted on a beaker. The 3DP MoS_2-SS catalyst was fixed on a mechanical agitator with a rotation speed of 500 r/min. The initial pH value was regulated by 50 mmol/L NaOH and H_2SO_4 solution. Quenching experiments using different quenching agents were exhibited to investigate the role of radical oxygen species (ROS) on the degradation of FLO. At certain time intervals, 1 mL sample solution was collected from the beaker and filtered through a 0.22 μm polyether sulfone membrane for the analysis of FLO concentration. Influencing factors such as initial PMS concentration (0-1.5 mmol/L), initial pH value (3.1-9.0) on the effect of degradation performance were optimized. In addition, we evaluated the degradation performance of various organic pollutants such as 2-CP, CBZ, IBP and ACT. The solution volume, initial organics concentration and reaction temperature were set as 100 mL, 10 mg/L and 25°C, respectively.

1.4. *Analytical methods*

The high performance liquid chromatography (HPLC, LC-16, Shimadzu, Japan) was used for the analysis of organic compounds, and the detailed parameters were listed in **Appendix A Table S1**). The degradation products of FLO were analyzed by UPLC/MS, and the details were present in our previous work (Xu et al., 2022a). TOC concentration, aqueous inorganic anion (Cl^-, F^-) were determined by TOC analyzer (Elementar, Germany), ion chromatography (Dionex ICS-5000, Thermo Fisher Scientific, UK) with an electron capture detector, respectively.

The microstructure and crystalline structure of 3DP MoS_2-SS were characterized by scanning electron microscop (SEM, Hitachi SU-5000+ Oxford Instruments Ultim Max, Hitachi Ltd., Chiyoda-ku, Japan) and X-ray diffraction (XRD, Rigaku Ultima IV, Rigaku Co., Japan), respectively. X-ray photoelectron spectroscopy (XPS, Thermo Scientific K-Alpha, Thermo Fisher Scientific, UK) was employed to investigated the elemental composition and electron structure of 3DP MoS_2-SS. Amperometric current-time curves was conducted to indicate the mechanism of PMS activation by 3DP MoS_2-SS, and 3DP MoS_2-SS, SS sheet and Ag/AgCl electrode were selected as the working electrode, counter electrode and reference electrode, respectively.

2. Results and discussion

2.1. *The characterization of 3DP MoS_2-SS*

The MoS_2-SS composite material was first synthesized by 3D printing method and the corresponding digital photographs were shown in **Appendix A Fig. S2**. The microstructure and morphology of 3DP MoS_2-SS were characterized by SEM (**Appendix A Fig. S3**). As shown in **Appendix A Fig. S3a** and **Appendix A Fig. S3b**, 3DP MoS_2-SS presented a 3D network skeleton structure and rough surface with a number of micropores, which was conducive to providing more active sites for catalytic reaction. Corresponding EDS mapping images indicated the homogeneous distribution of Mo, S, Fe, Mn and Cr elements on MoS_2-SS. The crystalline composition of 3DP MoS_2-SS was analyzed by XRD spectrum. As shown in **Appendix A Fig. S4**, 3DP MoS_2-SS demonstrates that the main diffraction peaks at 43.6, 50.8, 74.7 and 44.7° were assigned to the crystalline planes of (1 1 1), (2 0 0), (2 2 0) for austenite SS phase (JCPDS card#33-0397) and (1 1 0) for Fe (JCPDS card#06-0696), respectively. Moreover, Noted that there was no obvious crystal diffraction peak attributed to MoS_2 was found in the XRD spectrum of 3DP MoS_2-SS, which might be ascribed to high dispersion of MoS_2 during the 3D printing fabrication process. XPS analysis was employed to investigate the elemental composition and chemical state of the 3DP MoS_2-SS. As shown in **Appendix A Fig. S5**, the binding energy peaks of Fe, Mn, Cr, Mo, S, O and C were found in the XPS spectra of 3DP MoS_2-SS. The observation of Mo and S elements indicated the successful doping of MoS_2 on the SS. In the high resolution XPS spectra of Fe (**Appendix A Fig. S6**), the binding energy peaks at 707.2, 710.6, 713.8, 724.3 and 727.1 eV were corresponded to Fe^0 $2p_{3/2}$, Fe^{2+} $2p_{3/2}$, Fe^{3+} $2p_{3/2}$, Fe^{2+} $2p_{1/2}$ and Fe^{3+} $2p_{1/2}$, respectively, while the peaks at 719.6 and 733.0 eV were assigned to satellite peaks. The characteristic peaks centered at 229.2, 232.5 and 235.6 eV in the Mo spectra were attributed to Mo^{4+} $3d_{5/2}$, Mo^{4+} $3d_{3/2}$ and Mo^{6+} $3d_{3/2}$, respectively.

Electrochemical measure was employed to characterize the reactivity of 3DP SS and 3DP MoS_2-SS. As shown in Fig. 1**a**, the current response of 3DP MoS_2-SS was much higher than that of 3DP SS, implying that 3DP MoS_2-SS could provide more active sites for reaction (Yang et al., 2019). Our previous work also confirmed that the introduction of MoS_2 might greatly enhance the reaction active area of Ni substrate (Xu et al., 2022b). The capacity of electron transfer was evaluated by EIS and TPC analyses. In the EIS curves, the semi-diameter in the high frequency region represents the electron-transfer resistance (Rct) of the catalysts (Li et al., 2021a), and the equivalent circuit model for the simulation of the EIS data

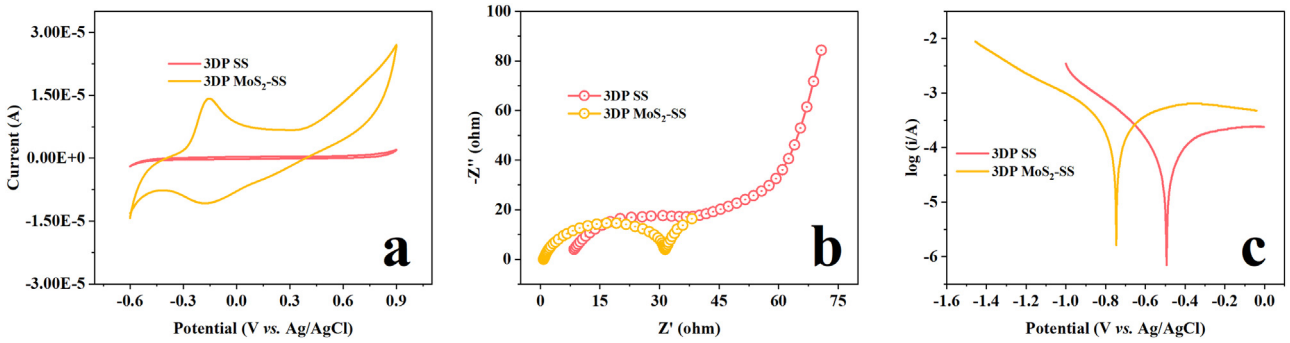

Fig. 1 – Electrochemical characterization of 3DP SS and 3DP MoS_2-SS. (a) CV. Experimental condition: 20 mmol/L Na_2SO_4 and applied potential ranged of -0.6-0.9 V *vs.* Ag/AgCl. (b) EIS. Experimental condition: amplitude voltage of 5 mV, frequency range of 0.01–10^5 Hz and 20 mmol/L Na_2SO_4. (c) TPC. Experimental condition: scan rate of 10 mV/sec and 20 mmol/L Na_2SO_4.

was presented in **Appendix A Fig. S7**. As displayed in Fig. 1b, the observed Rct in the EIS of 3DP SS and 3DP MoS_2-SS were 23.2 and 15.6 ohm, respectively. Noted that the introduction of MoS_2 on 3DP SS significantly decreased the Rct value, indicating MoS_2 could facilitate the electron-transfer rate of SS. Moreover, TPC results were consistent with the EIS analysis. Fig. 1c demonstrates that higher corrosion current (I_{corr}) of 3DP MoS_2-SS (0.191 mA) was found relative to 3DP SS (0.0734 mA). Taken together, the aforementioned results suggested the doping of MoS_2 on SS could significantly increase the active sites and electron-transfer rate.

2.2. *Catalytic performance of 3DP MoS_2-SS*

2.2.1. *Comparison of MoS_2-SS powder and 3DP MoS_2-SS*

The degradation performance of FLO was investigated to evaluate the catalytic ability of prepared catalysts. As shown in Fig. 2a and **Appendix A Fig. S8**, an inconspicuous amount of FLO was removed by MoS_2-SS or PMS alone, implying that the adsorption of catalysts and self-decomposition of PMS was not responsible for FLO degradation. However, the rapid degradation kinetics of FLO were found once the MoS_2-SS catalysts and PMS were applied simultaneously, and the degradation efficiencies of FLO were 98.89% and 98.69% in 20 min by MoS_2-SS powder and 3DP MoS_2-SS, respectively. The results demonstrated that both MoS_2-SS powder and 3DP MoS_2-SS could effectively activate PMS for FLO degradation. To clearly evaluate the utilization efficiency of active sites on the MoS_2-SS powder and 3DP MoS_2-SS, the normalized k_{FLO} by specific surface area (S_{BET}) were calculated. As shown in **Appendix A Fig. S9**, the S_{BET} of MoS_2-SS powder and 3DP MoS_2-SS were 0.9111 and 0.2134 m^2/g, respectively. However, the calculated k_{FLO}/S_{BET} of 3DP MoS_2-SS (1.60 g/(m^2/min)) was 4.3-fold than that of MoS_2-SS powder (0.37 g/(m^2/min)) (Fig. 2b). Although MoS_2-SS powder catalyst possessed a larger S_{BET} relative to massive catalysts, it might occur agglomeration and active sites on the surface would be covered during the catalytic reaction. This result indicated that 3DP MoS_2-SS could achieve efficient utilization of surface active sites for PMS activation and FLO degradation.

2.2.2. *The optimization of influencing factors*

The degradation efficiencies of FLO by 3DP SS and 3DP MoS_2-SS were investigated to elucidate the promoting function of

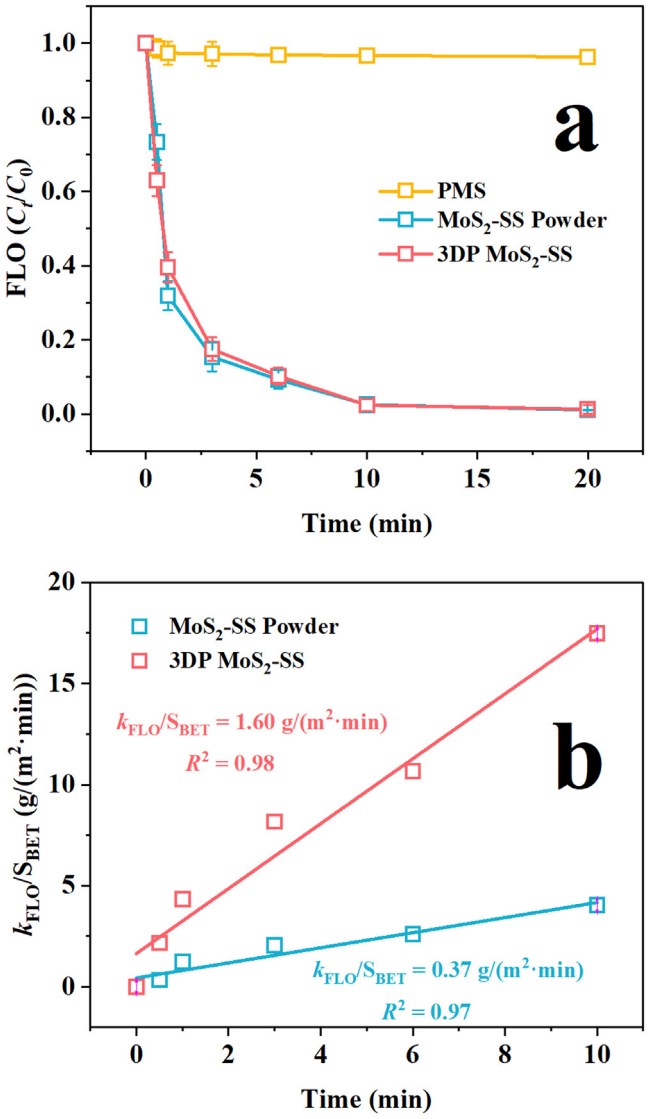

Fig. 2 – (a) The degradation performance of FLO by PMS, MoS_2-SS powder and 3DP MoS_2-SS. (b) k_{FLO}/S_{BET} of MoS_2-SS powder and 3DP MoS_2-SS. Experimental condition: 10 mg/L FLO and 1 mM PMS.

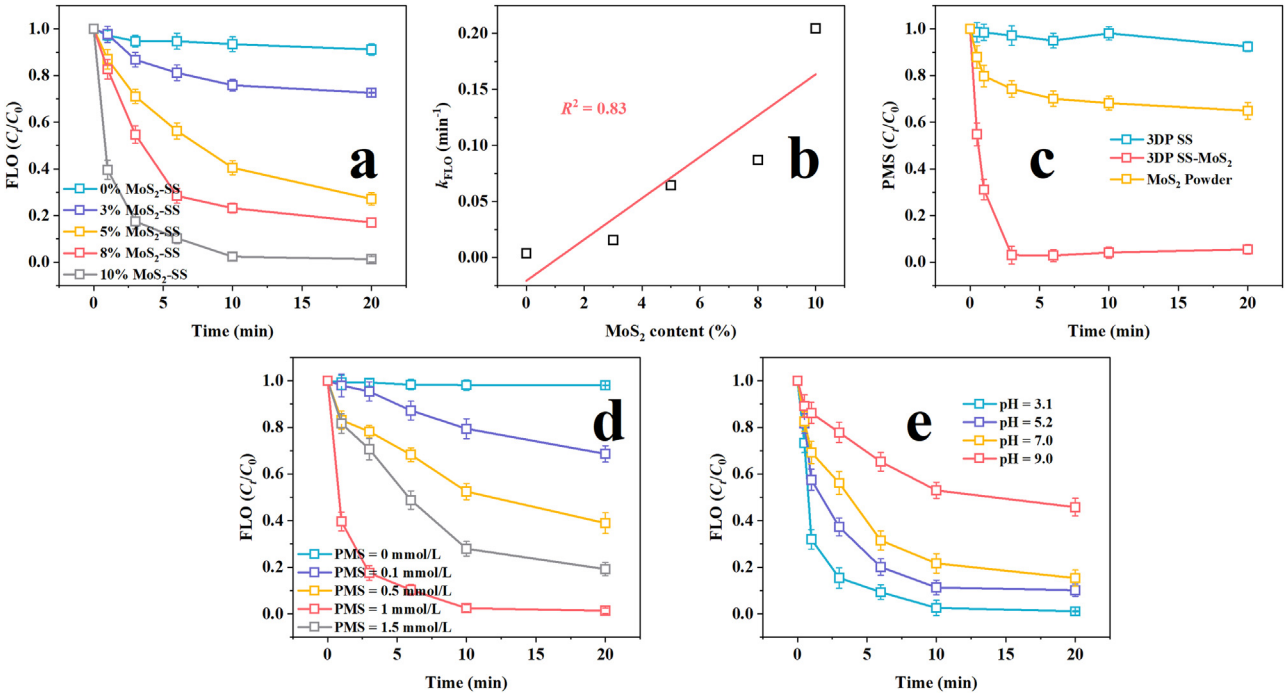

Fig. 3 – (a) The effect of MoS_2 content of 3DP MoS_2-SS toward the degradation of FLO, (b) Change patterns of k_{FLO} under different MoS_2 contents. (c) PMS decomposition performance in 3DP SS/PMS, MoS_2/PMS and 3DP MoS_2-SS/PMS systems. Influencing factors for the degradation of FLO by 3DP MoS_2-SS. (d) PMS dosage, (e) initial pH value. Experimental condition: 10 mg/L FLO and 1 mmol/L PMS.

MoS_2 doping for PMS activation and FLO degradation. As depicted in Fig. 3a, the degradation efficiencies of FLO were 8.84%, 27.42%, 72.88%, 82.96% and 98.69% as the MoS_2 content was 0, 3%, 5%, 8% and 10%, respectively. The degradation performance of FLO was in accord with the pseudo-first-order rate kinetics model, and k_{FLO} was proportional to the increasing doping content of MoS_2 (Fig. 3b). The k_{FLO} increased from 0.00382 to 0.20445 min^{-1} as the MoS_2 content increased from 0 to 10%. In this case, the variation of PMS concentration was measured during the sample periods to explain the important role of MoS_2. As shown in Fig. 3c, the decomposition of PMS by 3DP SS is less than 7% in 20 min, while it reaches 94.48% by 3DP MoS_2-SS. Since only MoS_2 could achieve PMS activation, but with a low efficiency (35.1%). Overall, the abovementioned results indicated that the doping of MoS_2 on SS facilitated the PMS activation and FLO degradation, which might be attributed to the effective utilization of active sites and enhanced interfacial electron transfer rate, as confirmed by CV, EIS and TPC analyses (Fig. 1). However, considering that MoS_2 was not a pure metal, it was inevitable that the increasing MoS_2 content on SS might be not conducive to the shaping of catalyst during the 3D printing technology. Thus, 10% MoS_2-SS was selected as a probe catalyst in the following experiments.

The effect of initial PMS dosage on the degradation performance of FLO by 3DP MoS_2-SS were investigated. As illustrated in Fig. 3d, the degradation efficiencies of FLO significantly increased from 1.99% to 98.69% as the PMS concentration raised from 0 to 1 mmol/L, due to the increased ROS generation during the PMS activation. However, an obvious inhibition in the degradation efficiency of FLO was found as PMS concentration increased to 1.5 mmol/L. This phenomenon could be attributed to the competing reaction between PMS and ROSs, which was consistent with the previous study (Wang et al., 2022b; Yu et al., 2021). Thus, the PMS dosage of 1 mmol/L was selected for the following experiments. Fig. 3e exhibits the effects of initial pH (3.0-9.0) on FLO degradation. We observed acidic pH favored the degradation of FLO. It was well known that various metal ions (e.g., Fe, Mo) might dissolve into the solution at an acidic pH value for PMS activation and alkaline pH would result in the passivation (Zhang et al., 2022a; Zhang et al., 2020).

2.3. *Activation mechanism of PMS by 3DP MoS_2-SS*

2.3.1. *Identification of ROSs*

Previous studies have declared that reactive radicals (e.g., •OH, SO_4•$^-$ and O_2•$^-$) could attack organics molecule and achieve rapid degradation in PMS-based AOPs (Huang et al., 2021; Li et al., 2022). Therefore, quenching tests were investigated to clarify the role of reactive radicals in 3DP MoS_2-SS/PMS system. As shown in Fig. 4a, the degradation efficiency obviously decreased to 16.72%, 10.71% and 29.31% with the addition of TBA, MeOH and BQ, respectively. It was well known that TBA, MeOH and BQ were considered as the quenching agents for •OH, both •OH and SO_4•$^-$, and O_2•$^-$, respectively, due to its high reactivity between quenching agents and reactive radicals (Xie et al., 2022). The remarkable inhibition effect of aforementioned quenching agents on FLO degradation indicated that both •OH, SO_4•$^-$ and O_2•$^-$ involved in the degradation process. Furthermore, EPR results were identical with that ob-

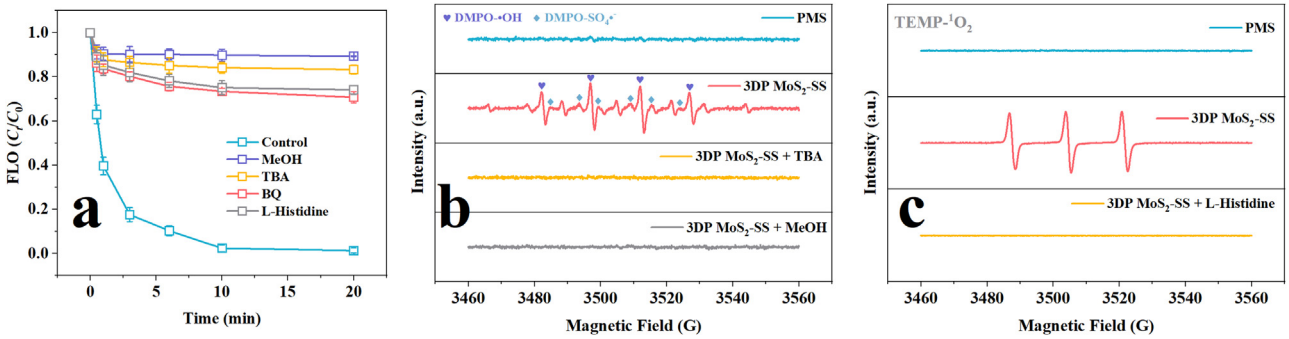

Fig. 4 – (a) Removal efficiency of FLO in 3DP MoS_2-SS/PMS system under different quenching conditions. (b) DMPO-•OH, DMPO-$SO_4^{\bullet-}$ adduct signals. (c) TEMP-$^1O_2$ adduct signals. Experimental condition: 10 mg/L FLO, 1 mmol/L PMS, 100 mmol/L DMPO and 100 mmol/L TEMP.

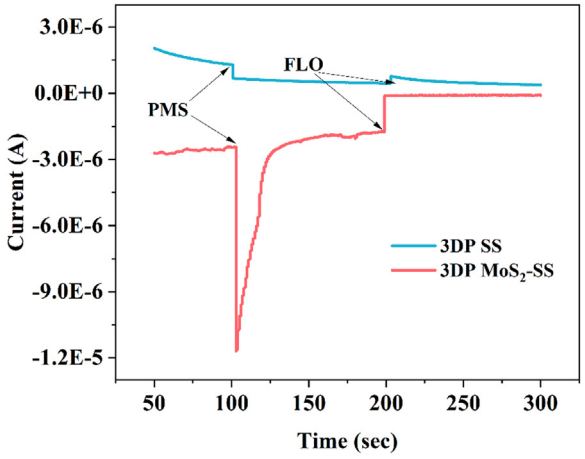

Fig. 5 – Amperometric current-time curves of 3DP MoS_2-SS. Experimental condition: 10 mg/L FLO and 1 mM PMS.

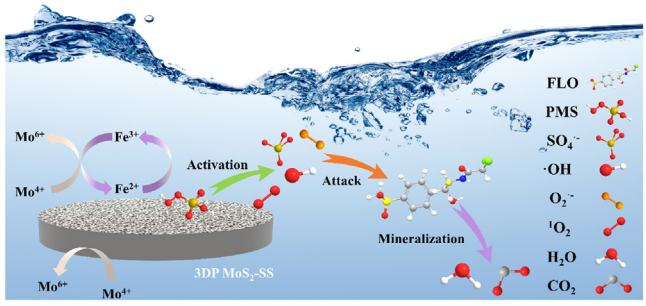

Fig. 6 – Schematic diagram of FLO degradation in 3DP MoS_2-SS/PMS system.

tained by quenching experiments (Fig. 4**b-c**). Both DMPO-•OH and DMPO-$SO_4^{\bullet-}$ adduct signals were observed in the EPR spectra and disappeared as the addition of TBA and MeOH. In addition, other ROSs such as $^1O_2$ might also be generated during the PMS activation process (Fu et al., 2022; Wu et al., 2021). The obtained TEMP-$^1O_2$ adduct signals in the EPR spectra confirmed the existence of $^1O_2$, and the degradation efficiency decreased from 98.69% to 25.97% in the presence of L-histidine (as a trapping agent for $^1O_2$), indicating that nonradical oxidation pathway dominated by $^1O_2$ also participated in the FLO degradation. Overall, quenching experiments and EPR analyses indicated both radical and nonradical oxidation pathway were responsible for FLO degradation.

2.3.2. *Electrochemical measurement and XPS analysis*

Electrochemical measurement was applied to explore the mechanism of PMS activation by 3DP MoS_2-SS. As shown in Fig. 5, as the addition of PMS, the significant decrease of the current response in the amperometric current-time curve indicates that the electron transfer occurred between PMS and 3DP MoS_2-SS. 3DP SS also demonstrated similar variations of current response like 3DP MoS_2-SS. Noted that more remarkable increase in the current response was achieved by 3DP MoS_2-SS, further implying the doping of MoS_2 could accelerate the PMS activation and organics degradation process.

To elucidate the specific mechanism of PMS activation in 3DP MoS_2-SS/PMS system, the variations of elemental chemical state before and after treatment were investigated by XPS analyses. As shown in **Appendix A Fig. S6a**, the characteristic peaks of Fe^0 disappeared after the treatment, indicating that surface Fe^0 on the 3DP MoS_2-SS were involved in the PMS activation and FLO degradation processes. Previous studies demonstrated that Fe° could directly activate PMS to generate a great quantity of ROSs for organics degradation (Zhang et al., 2022a). It can be found that the intensity of Fe^{2+} decreased from 50.3% to 46.3%, while the intensity of Fe^{3+} increased from 28.0% to 30.4% after the catalytic reaction. This result suggested that the transformation of Fe species participated in the 3DP MoS_2-SS/PMS system (Eqs. (1)-(2)). The XRD results before and after treatment also confirmed this conclusion (**Appendix A Fig. S10**), the intensity of Fe significantly decreased after the degradation process. In addition, the valent state of Mo elements on the 3DP MoS_2-SS underwent an obvious change, in which the ratio of Mo^{4+} to total Mo decreased from 90.3% to 75.2% and that of Mo^{6+} increased from 9.7% to 24.8%. Based on our experiments and reported study, the role of Mo can be divided into the following two parts (Fig. 6). Firstly, the transformation of Mo^{4+}/Mo^{6+} could directly mediate the PMS activation to generate ROSs (Eq. (3)). More importantly, Mo^{4+}/Mo^{6+} could retain the redox properties of Fe,

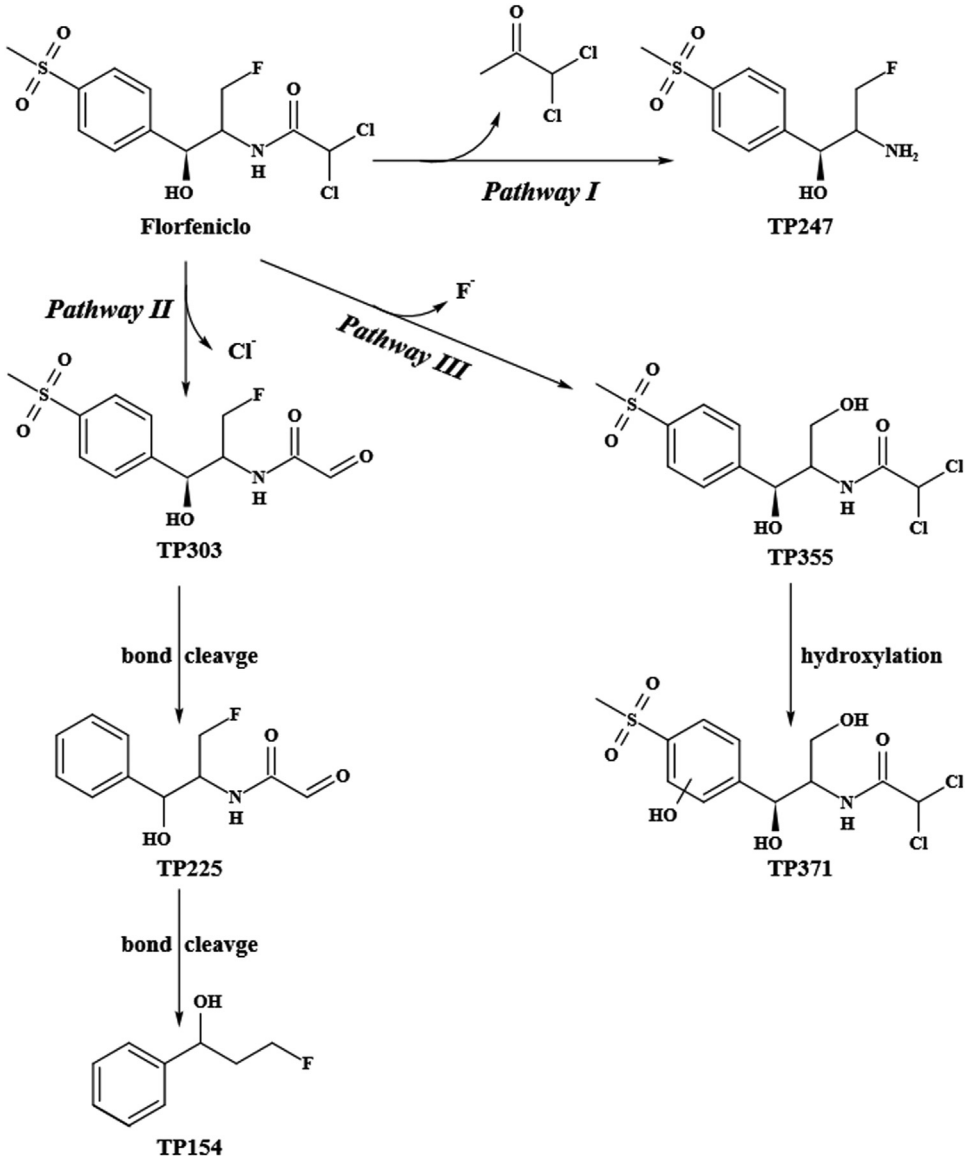

Fig. 7 – The possible degradation pathways of FLO in 3DP MoS_2-SS/PMS system.

in which Mo^{4+} provided electrons for the cycle of Fe^{2+}/Fe^{3+} (Eq. (4)) and accelerated the PMS activation process (Lu et al., 2021; Yi et al., 2019).

$$Fe^{2+} + HSO_5^- \rightarrow Fe^{3+} + OH^- + SO_4\bullet^- \quad (1)$$

$$Fe^{2+} + HSO_5^- \rightarrow Fe^{3+} + \bullet OH + SO_4^{2-} \quad (2)$$

$$Mo^{4+} + 2HSO_5^- \rightarrow Mo^{6+} + 2\bullet OH + 2SO_4\bullet^- \quad (3)$$

$$Mo^{4+} + 2Fe^{3+} \rightarrow Mo^{6+} + 2Fe^{2+} \quad (4)$$

2.4. *Degradation mechanisms and stability analysis*

The degradation products of FLO in 3DP MoS_2-SS/PMS were determined by UPLC/MS analysis (Fig. 7). Six degradation products were detected and three possible degradation pathways were proposed as follows: (i) the cleavage of C-N bonds resulted in the formation of TP247, (ii) dechlorination and then hydrolysis, subsequently cleavage of C-N bonds led to the formation of TP154, (iii) defluorination and hydroxylation of benzene ring to generate TP371. Furthermore, the degradation products might undergo effective mineralization to inorganic small molecule (e.g., CO_2, H_2O, Cl^-, F^-, etc.). As shown in Fig. 8**a**, the TOC removal efficiency was 90.2% and the concentrations of Cl^- and F^- were 0.73 mg/L and 0.56 mg/L at 20 min of reaction, respectively, indicating that 3DP MoS_2-SS/PMS system could achieve effective mineralization of FLO. In addition, the recycle performance was an essential factor to evaluate the applicability and compatibility of catalyst. Thus, the recycle degradation experiments of 3DP MoS_2-SS and MoS_2-SS powder catalyst for FLO degradation were evaluated (Fig. 8**b** and **Appendix A Fig. S11**). The degradation efficiency of FLO by MoS_2-SS powder catalyst significantly decreased from 98.89% to 68.85% after forth cycles, while it was

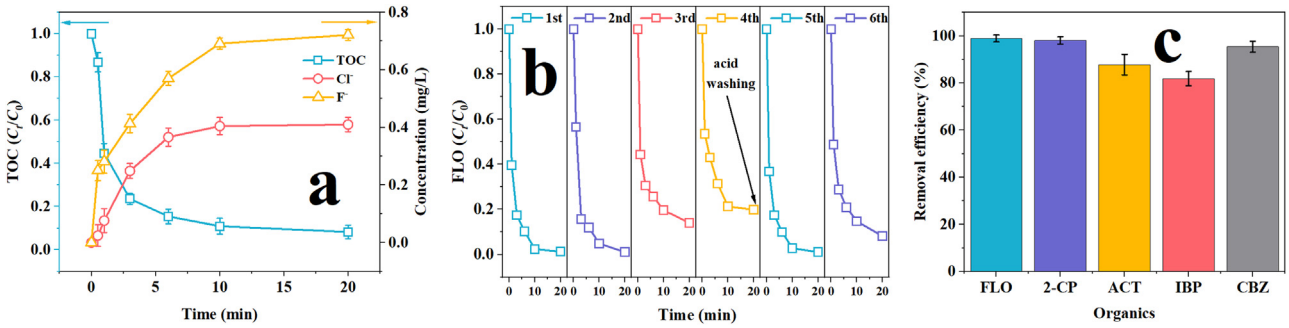

Fig. 8 – (a) TOC removal efficiency, the detected concentrations of Cl^- and F^-, Experimental condition: 10 mg/L FLO and 1 mmol/L PMS. (b) recycle performance of 3DP MoS_2-SS towards FLO degradation. (c) Removal efficiency of various organics in 3DP MoS_2-SS/PMS system. Experimental condition: 10 mg/L organics and 1 mmol/L PMS.

only decreased from 98.69% to 80.1% by 3DP MoS_2-SS. Obviously, the result indicated that MoS_2-SS fabricated by 3D printing method possessed superior stability toward FLO degradation compared with MoS_2-SS powder. Moreover, iron oxide and hydroxide would be inevitably formed on the catalyst surface during the treatment process, resulting in the low reactivity toward organics degradation. 3DP MoS_2-SS would maintain excellent degradation performance to FLO after a simple acid-washing process, implying that 3DP MoS_2-SS has a good practical application prospect in wastewater treatment. To comprehensively evaluate the applicability and safety of 3DP MoS_2-SS, the concentration of metal ions in the solutions after treatment were detected by ICP-MS analyses. As shown in **Appendix A Fig. S12**, the dissolved concentrations of Cr, Fe, Mn, Mo and Ni were 0.03, 0.17, 0.03, 0.06 and 0.01 mg/L, respectively, which were lower than the drinking water ordinance limit of world health organization. Therefore, it was safe to utilize 3DP MoS_2-SS massive catalyst for the FLO-polluted water treatment. In addition, the removal performance of various organics (i.e., 2-CP, ACT, IBP and CBZ) in 3DP MoS_2-SS/PMS system were conducted (Fig. 8**c**). The degradation efficiency of 2-CP, ACT, IBP and CBZ were 98.1%, 87.8%, 81.9%, 95.4%, respectively. The abovementioned results demonstrated that prepared 3DP MoS_2-SS in this study could be widely applied for PMS activation and the treatment of aqueous various organics.

3. Conclusion

In this study, a novel MoS_2-SS composite material was synthetized via a 3D printing method. Compared with MoS_2-SS powder, 3DP MoS_2-SS achieved superior utilization of active sites for PMS activation and FLO degradation, and the calculated k_{FLO}/S_{BET} of 3DP MoS_2-SS (1.60 g/(m^2/min)) was 4.3-fold than that of MoS_2-SS powder (0.37 g/(m^2/min)). The doping of MoS_2 facilitated the electron transfer rate and provide more active sites, and The k_{FLO} increased from 0.00382 to 0.20445 min^{-1} as the MoS_2 content increased from 0 to 10%. In addition, Mo^{4+} could provide electrons for the cycle of Fe^{2+}/Fe^{3+}. Quenching experiments and EPR measurement indicated that •OH, SO_4•$^-$, O_2•$^-$ and $^1O_2$ were involved in the degradation of FLO. Various influencing factors such as initial PMS dosage and pH value were optimized, and the optimized degradation efficiency of 98.69% was achieved at 1 mmol/L PMS and pH of 3.0. In addition, the possible degradation pathways of FLO were proposed to be the cleavage of C-N bonds, dechlorination, hydrolysis, defluorination and hydroxylation. 3DP MoS_2-SS could maintain superior catalytic performance toward PMS activation and organics degradation after a simple acid washing. Overall, this study demonstrated that 3DP MoS_2-SS could efficiently activate PMS for organics degradation relative to MoS_2-SS powder and provided an understanding of Fe-based catalyst prepared by 3D printing for the treatment of aqueous organics.

Declaration of Competing Interest

The authors declare no competing financial interest.

Acknowledgments

This study was supported by the Guangdong Province Enterprise Science and Technology Commissioner Project (No. GDKTP2021048000), the National Natural Science Foundation of China (No. 41907292), the Guangdong Basic and Applied Basic Research Foundation (No. 2019A1515110497), the Key-Area Research and Development Program of Guangdong Province (No. 2020B090923002) and the Guangdong Basic and Applied Basic Research Foundation (No. 2019B1515130005).

Appendix A Supplementary data

Supplementary material associated with this article can be found, in the online version, at doi:10.1016/j.jes.2023.01.016.

References

Bahmani-Oskooee, M., Hossein Nedjad, S., Samadi, A., Kozeschnik, E., 2017. Cu-bearing, martensitic stainless steels for applications in biological environments. Mater. Des. 130, 442–451.

Cao, J., Lai, L., Lai, B., Yao, G., Chen, X., Song, L., 2019. Degradation of tetracycline by peroxymonosulfate activated with zero-valent iron: Performance, intermediates, toxicity and mechanism. Chem. Eng. J. 364, 45–56.
Chen, X., Li, S., Yang, P., Chen, Y., Xue, C., Long, Y., et al., 2022. N-doped carbon intercalated Fe-doped MoS_2 nanosheets with widened interlayer spacing: an efficient peroxymonosulfate activator for high-salinity organic wastewater treatment. J. Colloid Interface Sci. 628 (Pt A), 318–330.
Chu, C., Yang, J., Zhou, X., Huang, D., Qi, H., Weon, S., et al., 2021. Cobalt single atoms on tetrapyridomacrocyclic support for efficient peroxymonosulfate activation. Environ. Sci. Technol. 55 (2), 1242–1250.
Ding, H., Zhu, Y., Wu, Y., Zhang, J., Deng, H., Zheng, H., et al., 2020. In Situ regeneration of phenol-saturated activated carbon fiber by an Electro-peroxymonosulfate process. Environ. Sci. Technol. 54 (17), 10944–10953.
Fu, F., Cheng, Z., Dionysiou, D.D., Tang, B., 2015. Fe/Al bimetallic particles for the fast and highly efficient removal of Cr(VI) over a wide pH range: performance and mechanism. J. Hazard. Mater. 298, 261–269.
Fu, J., Feng, L., Liu, Y., Zhang, L., Li, S., 2022. Electrochemical activation of peroxymonosulfate (PMS) by carbon cloth anode for sulfamethoxazole degradation. Chemosphere 287 (Pt 2), 132094–132104.
Gao, B., Zhu, S., Gu, J., Liu, Y., Yi, X., Zhou, H., 2022. Superoxide radical mediated Mn(III) formation is the key process in the activation of peroxymonosulfate (PMS) by Mn-incorporated bacterial-derived biochar. J. Hazard. Mater. 431, 128549–128560.
Huang, L., Zeng, T., Xu, X., He, Z., Chen, J., Song, S., 2019. Immobilized hybrids between nitrogen-doped carbon and stainless steel derived Fe_3O_4 used as a heterogeneous activator of persulfate during the treatment of aqueous carbamazepine. Chem. Eng. J. 372, 862–872.
Huang, M., Wang, X., Liu, C., Fang, G., Gao, J., Wang, Y., et al., 2021. Mechanism of metal sulfides accelerating Fe(II)/Fe(III) redox cycling to enhance pollutant degradation by persulfate: Metallic active sites vs. reducing sulfur species. J. Hazard. Mater. 404 (Pt B), 124175–124186.
Huo, X., Zhou, P., Liu, Y., Cheng, F., Liu, Y., Cheng, X., et al., 2020. Removal of contaminants by activating peroxymonosulfate (PMS) using zero valent iron (ZVI)-based bimetallic particles (ZVI/Cu, ZVI/Co, ZVI/Ni, and ZVI/Ag). RSC Adv 10 (47), 28232–28242.
Lee, C.-Y., Taylor, A.C., Beirne, S., Wallace, G.G., 2017. 3D-Printed conical arrays of TiO_2 electrodes for enhanced photoelectrochemical water splitting. Adv. Energy Mater. 7 (21).
Li, D., Zhong, Y., Wang, H., Huang, W., Peng, P., 2021a. Remarkable promotion in particle dispersion and electron transfer capacity of sulfidated nano zerovalent iron by coating alginate polymer. Sci. Total Environ. 759, 143481–143493.
Li, H., Yang, W., Ma, L., Liu, G., Yu, Y., Cao, J., et al., 2021b. 3D-printed highly ordered Ti networks-based boron-doped diamond: an unprecedented robust electrochemical oxidation anode for decomposition of refractory organics. Chem. Eng. J. 426, 131479–131490.
Li, M., Jin, Y.T., Cao, D.Y., Yang, L.L., Yan, J.F., Zhang, Z.X., et al., 2022. Efficient decomposition of perfluorooctane sulfonate by electrochemical activation of peroxymonosulfate in aqueous solution: Efficacy, reaction mechanism, active sites, and application potential. Water Res 221, 118778–118789.
Liang, H., Yu, M., Guo, J., Zhan, R., Chen, J., Li, D., et al., 2021. A novel vacancy-strengthened Z-scheme g-C_3N_4/Bp/MoS_2 composite for super-efficient visible-light photocatalytic degradation of ciprofloxacin. Sep. Purif. Technol. 272.
Lu, J., Zhou, Y., Zhou, Y., 2021. Efficiently activate peroxymonosulfate by Fe_3O_4@MoS_2 for rapid degradation of sulfonamides. Chem. Eng. J. 422.
Ma, W., Xu, X., An, B., Zhou, K., Mi, K., Huo, M., et al., 2021. Single and ternary competitive adsorption-desorption and degradation of amphenicol antibiotics in three agricultural soils. J. Environ. Manage. 297, 113366–113375.
Pang, Y., Ruan, Y., Feng, Y., Diao, Z., Shih, K., Hou, L., et al., 2019. Ultrasound assisted zero valent iron corrosion for peroxymonosulfate activation for Rhodamine-B degradation. Chemosphere 228, 412–417.
Shi, Y., Zhou, Y., Yang, D.R., Xu, W.X., Wang, C., Wang, F.B., et al., 2017. Energy level engineering of MoS_2 by transition-metal doping for accelerating hydrogen evolution reaction. J. Am. Chem. Soc. 139 (43), 15479–15485.
Son, A., Lee, J., Lee, C., Cho, K., Lee, J., Hong, S.W., 2021. Persulfate enhanced photoelectrochemical oxidation of organic pollutants using self-doped TiO_2 nanotube arrays: effect of operating parameters and water matrix. Water Res 191, 116803–116811.
Sullivan, I., Zhang, H., Zhu, C., Wood, M., Nelson, A.J., Baker, S.E., et al., 2021. 3D printed Nickel-Molybdenum-based electrocatalysts for hydrogen evolution at low overpotentials in a flow-through configuration. ACS Appl. Mater Interfaces 13 (17), 20260–20268.
Wang, M.M., Liu, L.J., Wen, J.T., Ding, Y., Xi, J.R., Li, J.C., et al., 2022a. Multimetallic CuCoNi oxide nanowires in situ grown on a nickel foam substrate catalyze persulfate activation via mediating electron transfer. Environ. Sci. Technol. 12613–12624.
Wang, S.-D., He, L.-X., Zhou, L., Xian, S.-D., Liu, J.-H., 2022b. Electrochemical activation of peroxymonosulfate with titanium suboxide anode for 4-chlorophenol degradation: Influencing factors, kinetics, and degradation mechanism. Sep. Purif. Technol. 291, 120964–120973.
Wu, L., Sun, Z., Zhen, Y., Zhu, S., Yang, C., Lu, J., et al., 2021. Oxygen vacancy-induced Nonradical degradation of organics: critical trigger of oxygen (O_2) in the Fe-Co LDH/Peroxymonosulfate system. Environ. Sci. Technol. 55 (22), 15400–15411.
Xie, Z.H., He, C.S., Zhou, H.Y., Li, L.L., Liu, Y., Du, Y., et al., 2022. Effects of molecular structure on organic Contaminants' degradation efficiency and dominant ROS in the advanced oxidation process with multiple ROS. Environ. Sci. Technol. 8784–8795.
Xu, J., Liu, Y., Li, D., Li, L., Zhang, Y., Chen, S., et al., 2022a. Insights into the electrooxidation of florfenicol by a highly active La-doped Ti_4O_7 anode. Sep. Purif. Technol. 291, 120904–120914.
Xu, J., Wang, P., Chen, S., Li, L., Li, D., Zhang, Y., et al., 2022b. 3D-printed MoS_2/Ni electrodes with excellent electro-catalytic performance and long-term stability for dechlorination of florfenicol. J. Environ. Sci..
Yang, Z., Lv, X., Zhang, C., Zhang, Y., Jia, S., Niu, Y., et al., 2021a. Core-sheath 3D printing of highly conductive and MoS_2-loaded electrode with pseudocapacitive behavior. Chem. Eng. J. 423, 130304–130312.
Yang, C., Zhang, C., Chen, Z.J., Li, Y., Yan, W.Y., Yu, H.B., et al., 2021b. Three-dimensional hierarchical porous structures of metallic Glass/Copper composite catalysts by 3D printing for efficient wastewater treatments. ACS Appl Mater Interfaces 13 (6), 7227–7237.
Yang, Z., Yang, X., Yang, T., Cao, Y., Zhang, C., Zhang, Y., et al., 2023. 3D printing of carbon tile-modulated well-interconnected hierarchically porous pseudocapacitive electrode. Energy Stor. Mater. 54, 51–59.
Yang, L., Chen, Z., Cui, D., Luo, X., Liang, B., Yang, L., et al., 2019. Ultrafine palladium nanoparticles supported on 3D self-supported Ni foam for cathodic dechlorination of florfenicol. Chem. Eng. J. 359, 894–901.

Yao, Y., Hu, H., Yin, H., Yu, M., Zheng, H., Zhang, Y., et al., 2020. Phase change on stainless-steel mesh for promoting sulfate radical formation via peroxymonosulfate oxidation. Appl. Catal. B: Environ. 278.

Yi, Q., Ji, J., Shen, B., Dong, C., Liu, J., Zhang, J., et al., 2019. Singlet oxygen triggered by superoxide radicals in a Molybdenum Cocatalytic fenton reaction with enhanced REDOX activity in the environment. Environ. Sci. Technol. 53 (16), 9725–9733.

Yu, L.Q., Zhao, Y.H., Wang, H., Jin, F., Chen, S.L., Wen, T.E., et al., 2021. Surface oxygen vacancies formation on Zn_2SnO_4 for bisphenol-A degradation under visible light: the tuning effect by peroxymonosulfate. J. Hazard. Mater. 127828–127836.

Zhang, D., Kong, X., Jiang, M., Lei, D., Lei, X., 2019a. NiOOH-Decorated α-FeOOH nanosheet array on stainless steel for applications in oxygen evolution reactions and supercapacitors. ACS Sustain. Chem. Eng. 7 (4), 4420–4428.

Zhang, K., Liu, Y., Wang, B., Yu, F., Yang, Y., Xing, L., et al., 2019b. Three-dimensional interconnected MoS_2 nanosheets on industrial 316L stainless steel mesh as an efficient hydrogen evolution electrode. Int. J. Hydrogen Energy 44 (3), 1555–1564.

Zhang, Y.-f., Zhang, C.-h., Liu, Y.-f., Li, D., Xu, J.-h., Li, L., et al., 2022a. Fast degradation of florfenicol in SiC-Fe° Fenton-like process: the overlooked role of atomic H* in peroxymonosulfate activation. Sep. Purif. Technol. 303, 122187–122197.

Zhang, Y.-f., Zhang, C.-h., Xu, J.-h., Li, L., Li, D., Wu, Q., et al., 2022b. Strategies to enhance the reactivity of zero-valent iron for environmental remediation: a review. J. Environ. Manag. 317, 115381–115387.

Zhang, Y., Niu, J., Xu, J., 2020. Fe(II)-promoted activation of peroxymonosulfate by molybdenum disulfide for effective degradation of acetaminophen. Chem. Eng. J. 381, 122718–122725.

Zhou, X., Jing, G., Lv, B., Zhou, Z., Zhu, R., 2016. Highly efficient removal of chromium(VI) by Fe/Ni bimetallic nanoparticles in an ultrasound-assisted system. Chemosphere 160, 332–341.

Zhou, Y., Wang, X., Zhu, C., Dionysiou, D.D., Zhao, G., Fang, G., et al., 2018. New insight into the mechanism of peroxymonosulfate activation by sulfur-containing minerals: role of sulfur conversion in sulfate radical generation. Water Res 142, 208–216.